11th International Workshop on Ship and Marine Hydrodynamics
Hamburg, Germany, September 22-25, 2019

Numerical Study on Influencing Factors of High Speed Water Entry

Shiming Sun*, Kai Yan, Xiaohui Wang, Guangtao Liu, Xuesen Chu

China Ship Scientific Research Center, National Key Lab of Science and Technology on Hydrodynamics
Shanshui East Road 222, 214082 Wuxi, China

*Corresponding author, ssm702@126.com

ABSTRACT

The accurate prediction of high speed water entry is very crucial for the research on improving the penetration abilities of underwater vehicles. In this paper, the water entry problem of an axisymmetric blunt vehicle with velocities ranging from 200m/s to 600m/s are numerically studied based on the CFD method. Firstly, the accuracy of the numerical method was verified by experiments. Secondly, the influence of water compressibility on the water entry is studied and it is found that the compressibility will affect impact loads of water entry but has little influence on cavity shapes. Thirdly, the numerical results of cavity shapes during early stages of water entry are compared with the theoretical results based on the principle of independence of the cavity sections expansion. It is found that the numerical results of cavity shape are generally agreed with theoretical results except for the parts near the water surface. Lastly, the main similarity parameters for high speed water entry are also analysed and it is concluded that Mach number is the most important similarity parameter during early stages of water entry at this range of velocities. The results of this paper could provide some guide for the numerical simulations and scaled tests of high-speed water entry.

1 INTRODUCTION

The problem of water entry of rigid bodies is an important area involved in the design of many kinds of underwater vehicles and platforms[1-2]. The velocity of water entry for conventional air-dropped torpedoes is in the order of tens of meters per second[3], which may be not high enough to avoid being intercepted. This leads to a great interest for the research of water entry at a higher velocity. However, high speed water entry problems are very different since the load characteristics and fluid dynamic phenomena are more complicated with strong nonlinearity and the water entry process is affected by many different parameters including vehicle geometry, fluid properties and impact parameters.

Von Karman[4] and Wagner[5] first conducted systematic theoretical analyses of water entry in the problem of sea plane water landing. Since then, many scholars have carried out researches on water entry of objects with different geometric shapes. For water entry of high speed vehicles, such as missiles and projectiles, numerical simulations and experimental modelling are major research tools in engineering practices since there is no perfect theoretical model for high speed water entry at present. However, the problem of water entry with velocities over 200m/s may be more complicated compared to the conventional water entry. For example, the water compressibility may play a role in high speed water entry and the similarity laws for the scaling experiments may also be different. These issues also attracted the interests of many scholars[6-10].

The purpose of this paper is to provide guidances for numerical simulations and scaling experiments of high speed water entry. We focus on some main factors which need to be considered in simulations and experiments of high speed water entry. The calculation was conducted to investigate the dynamical characteristics of an axisymmetric blunt vehicle when it enters water at velocities more than 200m/s by using a commercial CFD solver[11] combined with overset grids. The influence of water compressibility on the water entry, the cavity shapes and the main similarity parameters of high speed water entry are numerically studied, and the results are compared with theoretical or experimental results.

2 NUMERICAL METHOD

2.1 Governing Equations

The process of a high speed vehicle impacting on the water surface is simulated by solving the Reynolds-Averaged Navier-Stokes equations for unsteady flows. For the multi-phase flow solutions, the Volume of Fluid (VOF) multiphase model is employed to solve problems involving free surfaces. It can model several immiscible fluids by solving a single set of momentum equations and by tracking the volume fraction of each phase throughout the domain. The governing equations are written as follows:

$$\begin{cases} \dfrac{\partial \rho_m}{\partial t} + \dfrac{\partial}{\partial x_i}\left(\rho_m \bar{u}_i\right) = 0 \\ \dfrac{\partial}{\partial t}\left(\rho_m \bar{u}_j\right) + \dfrac{\partial}{\partial x_j}\left(\rho_m \bar{u}_i \bar{u}_j\right) = -\dfrac{\partial \bar{p}}{\partial x_j} + \dfrac{\partial}{\partial x_j}\left[\mu \dfrac{\partial \bar{u}_i}{\partial x_j} - \rho_m \overline{u_i' u_j'}\right] + \rho_m f_i \end{cases} \tag{1}$$

where $\rho_m = \sum a_k \rho_k$ is the mixture density; a_k and ρ_k are the volume fraction and density of the *k*th phase, respectively; $\bar{u}_i$ is the *i*th mean velocity component; f_i is the mass force; $\bar{p}$ is the fluid pressure; μ is the viscosity of the fluid, and $\rho_m \overline{u_i' u_j'}$ is the Reynolds stress.

2.2 Turbulence model

To close the governing equations, a turbulence model is needed. In this paper, different turbulence models are compared which will be discussed later in section (3.2) and the realizable *k-ε* turbulence model is selected in which transport equations for the turbulent kinetic energy *k* and its dissipation rate *ε* are solved to determine the turbulent viscosity. The transport equations for turbulent kinetic energy *k* and its dissipation rate *ε* can be written as:

$$\begin{cases} \dfrac{\partial (\rho k)}{\partial t} + \dfrac{\partial \left(\rho \bar{u}_j k\right)}{\partial x_i} = P - \rho\varepsilon + \dfrac{\partial}{\partial x_i}\left[\left(\mu + \dfrac{\mu_t}{\sigma_k}\right)\dfrac{\partial k}{\partial x_j}\right] \\ \dfrac{\partial (\rho \varepsilon)}{\partial t} + \dfrac{\partial \left(\rho \bar{u}_j \varepsilon\right)}{\partial x_i} = C_{\varepsilon 1}\dfrac{\varepsilon}{k}P - C_{\varepsilon 2}\rho\dfrac{\varepsilon^2}{k} + \dfrac{\partial}{\partial x_i}\left[\left(\mu + \dfrac{\mu_t}{\sigma_\varepsilon}\right)\dfrac{\partial \varepsilon}{\partial x_j}\right] \end{cases} \tag{2}$$

where $\mu_t = C_\mu k^2 / \varepsilon$ is the turbulence viscosity coefficient; $C_{\varepsilon 1}$, $C_{\varepsilon 2}$, σ_k and σ_ε are empirical coefficients, respectively.

2.3 Cavitation Model

The Schnerr-Sauer cavitation model is used in the calculation. The Schnerr-Sauer cavitation model is based on a reduced Rayleigh–Plesset equation and neglects the influence of bubble growth accelerations, viscous effects, and surface tension effects. The mass transfer rate per unit volume can be expressed as:

$$\dot{m} = n_0 a_l 4\pi \rho_g R^2 \frac{dR}{dt} \tag{3}$$

where n_0 is the number of bubbles per unit volume of liquid; a_l is the volume fraction of liquid; *R* is the local bubble radius which can be expressed as $R^3 = 4a_g / [n_0 3\pi(1 - a_g)]$; *dR/dt* is the bubble growth velocity, which is estimated using the inertia controlled growth model:

$$(\frac{dR}{dt})^2 = \frac{2}{3}\frac{P_{sat} - P_\infty}{\rho_l} \tag{4}$$

where P_{sat} is the saturation pressure corresponding to the temperature at the bubble surface; P_∞ is the pressure of the surrounding liquid, and ρ_l is the liquid density.

2.4 Tait equation

The Tait equation is employed in the simulation to describe the status of compressible liquid. The Tait equation without temperature correction is expressed as:

$$p = K_0\left[\left(\frac{\rho_l}{\rho_0}\right)^n - 1\right] + p_0 \tag{5}$$

where p_0 and ρ_0 are the reference pressure and reference density when the temperature is 273.15K; K_0 and n are the weak functions of temperature and pressure respectively, which are assumed as constants, $K_0 = 3\times10^8$, n=7.

The sound speed in water is defined as $a = \sqrt{\partial p / \partial \rho_l}$, and according to Eq. (5),

$$\frac{\partial p}{\partial \rho_l} = \frac{K_0 n}{\rho_0}(\frac{\rho_l}{\rho_0})^{n-1} \tag{6}$$

2.5 6-DOF Motion

The 6-DOF solver is used to deal with the motion of the vehicle. Fluid forces and moments acting on the vehicle are calculated by integrating the pressure and shear forces over the surfaces of the vehicle. The governing equation of the translating motion in the inertial coordinate system is:

$$\dot{\mathbf{V}}_g = \frac{1}{m}\sum \mathbf{f}_g \tag{7}$$

where $\dot{\mathbf{v}}_g$ is the translating acceleration of the mass center; m is the mass of the rigid body; $\mathbf{f}_g$ is the resultant force acting on the body.

The governing equation of the rotating motion is constructed in the body local coordinate system, as:

$$\dot{\mathbf{\Omega}} = L^{-1}(\sum \mathbf{M} - \mathbf{\Omega}\times L\mathbf{\Omega}) \tag{8}$$

where L is the tensor of the moments of inertia; $\mathbf{M}$ is the resultant moment acting on the body; $\mathbf{\Omega}$ is the angular velocity of the rigid body.

2.6 Numerical Discrete Method

The finite volume method is adopted to discretize the governing equations. The segregated flow solver is used to solve the integral conservation equations of mass and momentum which employs a pressure-velocity coupling algorithm of SIMPLE. The convection terms are discretized using a second order accurate upwind scheme and diffusion terms are discretized using a second order accurate central differencing scheme. The implicit time-stepping scheme is used for unsteady flows.

3 VERIFICATION OF THE CALCULATION METHOD

3.1 The Motion and Cavity Shape of Water Entry

In order to verify the accuracy of the numerical method in calculating the motion and cavity shape of water entry, experimental results for the high speed water entry of a slender axisymmetric projectile with flat nose shape are selected to compare with the calculation results. The experiment was conducted in a water tank for water entry and exit in CSSRC. The test model is 700mm long and 75mm in diameter. In the experiment, the model is pushed down from a certain height above the water surface at a speed of 200m/s. The overload of the model's motion is measured by an acceleration sensor and the cavity shape is recorded by high-speed video camera. The comparing result of cavities is shown in Fig.1. It can be seen that the penetration depth of water entry and the cavity shape at different moments are both agreed well, which prove the accuracy of the numerical method in calculating the motion and cavity shape of high speed water entry.

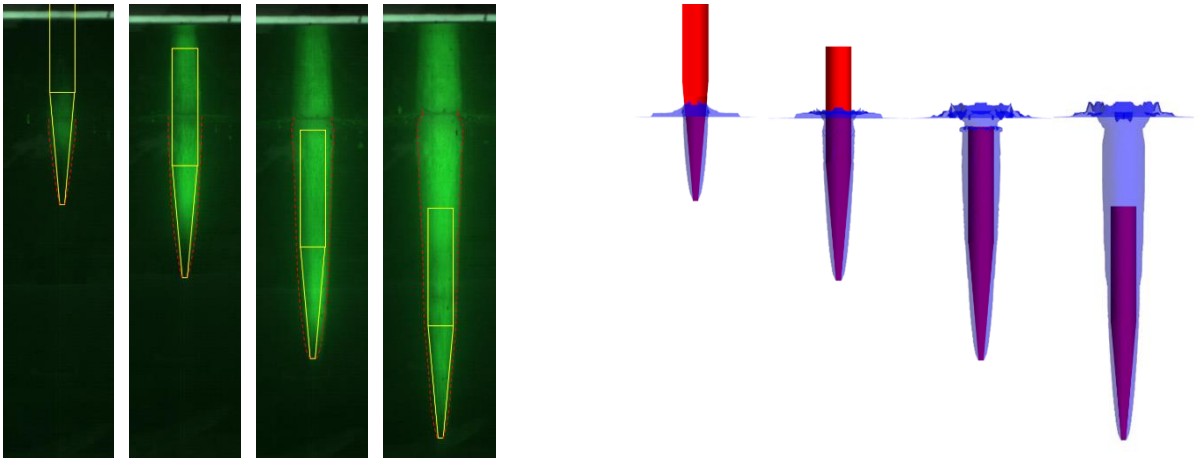

(a) Experimental results. (b) Numerical results.

Figure 1: Comparison of experimental and numerical results of water entry for a projectile.

3.2 Propagation of the Initial Shock Waves

When a vehicle impacts on the water surface with a high speed, energy is transferred into the water and causes a shock wave with a hemispherical wave front propagating in the water. McMillen[12] conducted a water entry experiment of a small steel sphere in which the microsecond spark shadowgraph method was used to show the shock waves in water. This paper chooses his experimental results to verify the ability of the numerical method to calculate the flow field caused by high speed impacts. The research object is a steel sphere which weighs 0.132g and has a diameter of 3.175mm. Fig. 2(e) shows the spark shadowgram of a wave caused by impacting after the sphere advancing 7.8 cm into the water with the velocity of 1073m/s. By comparing with the numerical results from different turbulence models, including the standard k-ε model, the realizable k-ε model, the standard k-ω model and the SST k-ω model, it can be seen that the propagation of the shock waves calculated using different turbulence models are almost the same except for the small differences where the water surface splashed and all simulation results agreed well with those in experiments.

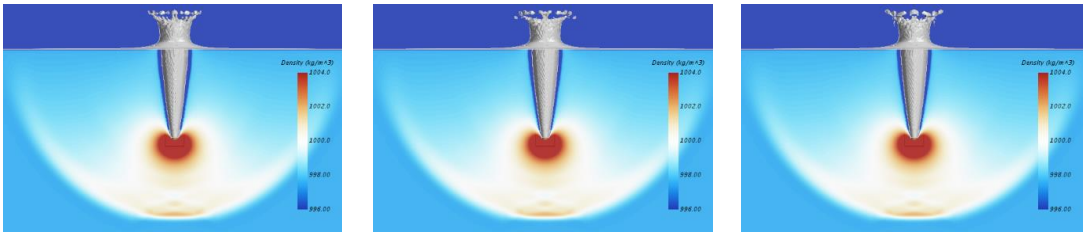

(a) Standard k-ε. (b) Realizable k-ε. (c) Standard k-ω.

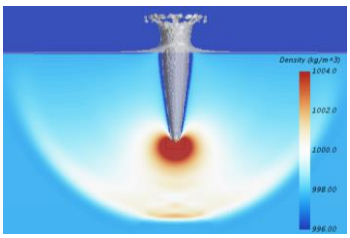

(d) SST *k-ω*.

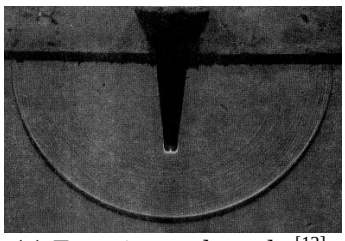

(e) Experimental results[12].

Figure 2: Propagation of shock waves calculated by different turbulence models.

As shown in Fig. 3, the cavity shapes from different turbulence model almost coincide by putting them in one picture for comparison. It can be concluded that the turbulence model has little effect on the calculation of the flow field, and their differences can be ignored for the study of cavity shapes at this velocity range.

By arranging various pressure monitoring points at different depths underwater in calculation, the peak pressure and the moment of the shock wave passing through each monitoring points can be obtained as shown in Fig.4. It can be seen that the shock waves propagate underwater at about the velocity of sound in water and the velocity decreases slightly with the increase of propagation distance. The peak pressure passing through each monitoring points decreases exponentially in a form of $y = 1 / x^{1.4}$.

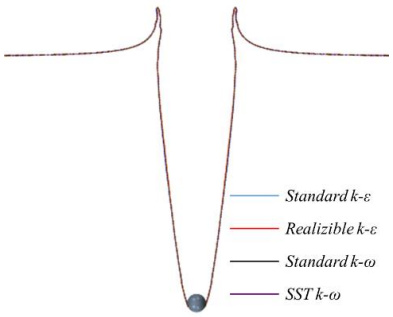

Figure 3: Comparison of cavity shapes for different turbulence models.

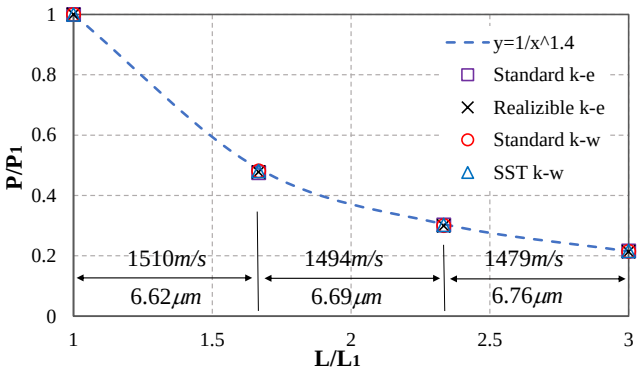

Figure 4: Non-dimensional peak pressure versus the sensor distance for different turbulence models. (P1 and L1 are the pressure and distance of the first monitor)

4 HIGH SPEED WATER ENTRY OF AN AXISYMMETRIC VEHICLE

4.1 Body and Domain for Calculation

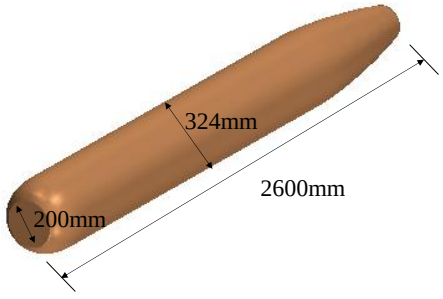

Figure 5: Dimensions of the calculation body

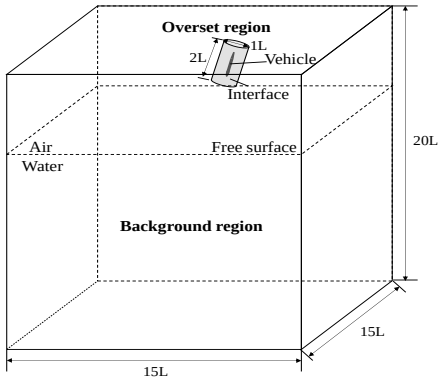

Figure 6: The schematic of computational domain.

The water entry body for calculation is an axisymmetric vehicle with a truncated-ogive-nosed shape and a contracted tail. The diameter of the vehicle is 324mm and the length is 2600mm[13], as shown in Fig. 5. The grids were generated with the overset grid method which is useful in problems dealing with multiple or moving bodies. The overset grid method is usually used to discretize a computational domain with several different grids that overlap each other. In this paper, the computational domain has two regions: the background region enclosing the entire solution domain and the smaller overset region containing the vehicle within the domain. Grids of computational domain are shown in Fig.6. All the boundaries of the background region is set as pressure boundary and the volume fraction of air and water on the boundary is determined according to the position of the free surface. The surface of the vehicle is set as the wall boundary and the outside surfaces of the overset region is set as the interface. The total number of grids is about 2.6 million.

4.2 Effect of Water Compressibility

Water compressibility can be ignored in most cases of water entry. However, for the velocity range this paper interested, water compressibility may play a role that cannot be ignored, though the Ma number based on sound speed in water is still lower than 0.3. Fig. 7 shows the comparison of the pressure fields at different moments in the process of water entry with and without consideration of water compressibility. The vehicle impacted on water surface at the velocity of 300m/s with the incidence angle of 80 °. When the water compressibility was considered, the water density has a positive correlation with pressure. After impacting with water, the shock wave was generated and propagated at the velocity close to the sound speed. Then, the shock wave will leave the high pressure area in the head region of the vehicle and form a spherical shock wave which propagates forward independently. In the process of propagation, the local density of water will increase, but its intensity will gradually weaken until it disappears. When the water compressibility is not considered, there is no such process of shock wave propagation as the water density is taken as constant.

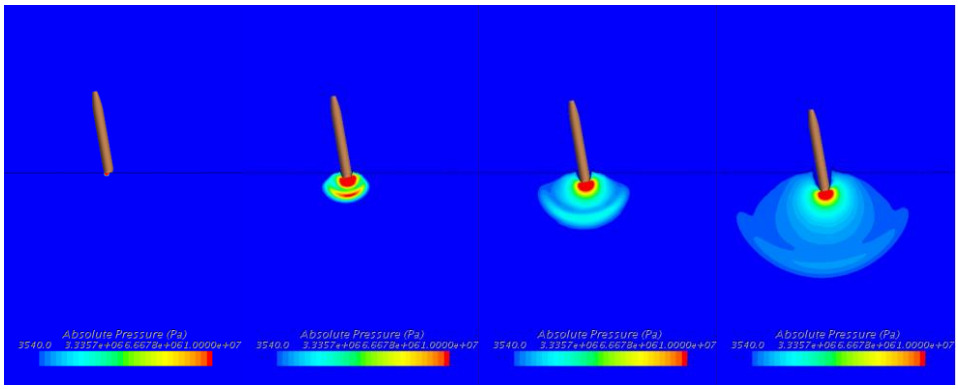

(a) Pressure fields for the vehicle impacting on the compressible water surface.

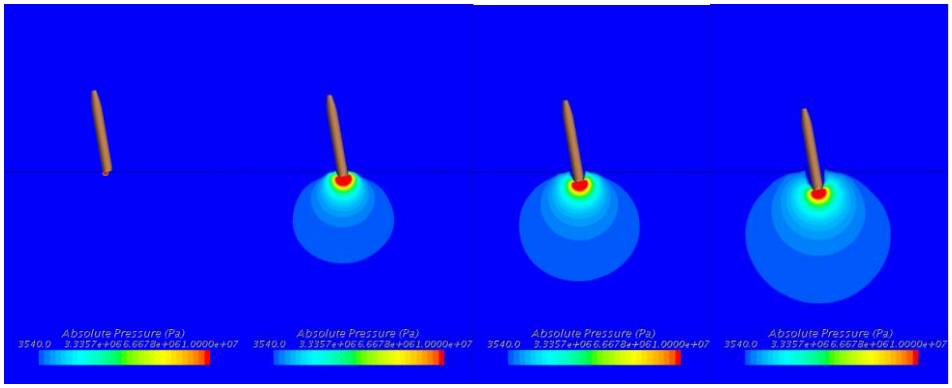

(b) Pressure fields for the vehicle impacting on the incompressible water surface.

Figure 7: Comparison of pressure fields with and without consideration of water compressibility.

Fig. 8-9 showed the comparisons of the impact loads and pitch angle versus time at the early stage of water entry for compressible and incompressible water, respectively. The peak load of the vehicle with

compressible water is lower than that with incompressible water, while the axil loads in the cavity-running phase are almost the same for both compressible and incompressible water. The time at pressure pulse in the compressible water is slightly longer than that in the incompressible water. The pitch angle of the vehicle will increase gradually under the action of moment caused by lateral force from water, that is, the vehicle will gradually deflect towards the head-up direction. The variation of the pitch angle with consideration of water compressibility is larger than that without consideration of water compressibility. However, from viewpoint of the cavity shape, whether or not the water compressibility is considered, it has no influence on the cavity profile, as shown in Fig. 10.

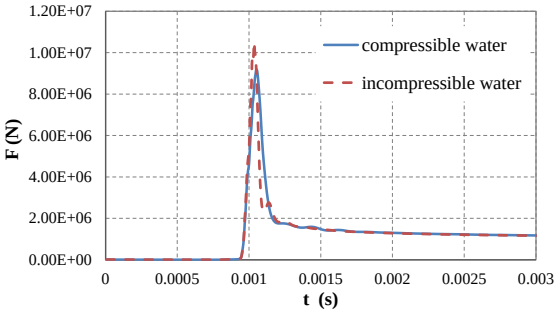

Figure 8: Comparison of impact loads for compressible and incompressible water.

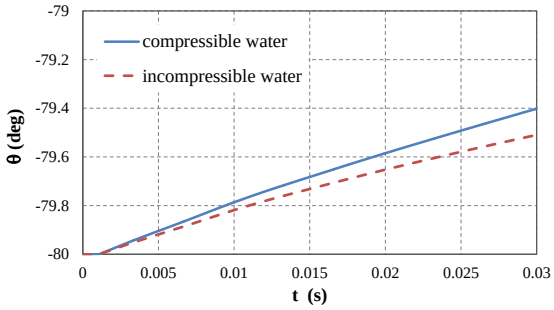

Figure 9: Comparison of pitch angle variation for compressible and incompressible water.

The impact accelerations at different velocities are compared as shown in Fig. 11. It can be seen that the influence of water compressibility on the impact acceleration becomes more evident with the increase of the impact velocity. Even when the velocity of water entry is 200m/s, the relative difference can be larger than 30%. It is believed that for the water entry at velocities over 200m/s, the influence of water compressibility on the vehicle acceleration should not be neglected, which also means that the its influence on the vehicle motion cannot be ignored.

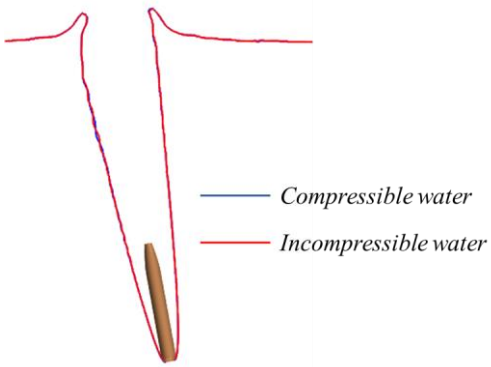

Figure 10: Comparison of cavity profile for compressible and incompressible water.

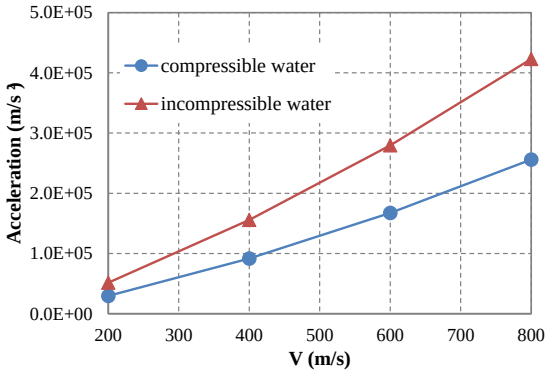

Figure 11: Comparison of impact accelerations for compressible and incompressible water at different velocities.

4.3 Influence of Free-surface on the Cavity Shape

In this section, the cavity shapes calculated in this paper during early stages of water entry are compared with the theoretical results based on the principle of independence of the cavity sections expansion[14]. In the theory, the cavity sections expansion is in the form of

$$\ddot{S} = -\frac{k\Delta P}{\rho_w} \tag{9}$$

where S is the area of a cavity cross section; ΔP is the difference between the pressure at infinity and the pressure in the cavity, and k is an empirical coefficient. By integrating Eq. (9) twice, the cavity section can be expressed as:

$$S(H_1,t) = S_0 + \dot{S}_0(t-t_1) - \frac{k}{\rho}\int_{t_1}^{t}\int_{t_1}^{u}\Delta P(H_1)\,du\,dt \tag{10}$$

where S_0 is the initial area of a cavity cross section; $\dot{S}_0$ is the initial velocity of expansion of the cavity section, and H_1 is the depth at the moment t_1. Other parameters can be written as follows:

$$\begin{cases} S_0 = \pi R_n^2,\ \dot{S}_0 = \dfrac{2\pi C_D R_n V(0)}{a} \\ C_D = C_{D0}(1+\sigma),\quad a = \sigma\dfrac{L_k}{2R_n} \\ \dfrac{L_k}{2R_n} = \sqrt{C_D\cdot\dfrac{1}{\sigma^2}\ln\dfrac{1}{\sigma}},\ k = \dfrac{4\pi C_{D0}(1+\sigma)}{a^2} \end{cases} \tag{11}$$

The simulations of the vehicle entering water at velocity of 300m/s were carried out and the results are compared with that in theory, as shown in Figure 12. It can be seen that numerical results of cavity shapes are generally agreed well with theoretical results except for the parts near the water surface. When the penetration depth is less than twice the body length, the size of cavity profiles is slightly smaller than theoretical results. The reason may be that the cavity shape is affected by the free surface at the initial stage of water-entry, which is not considered in the theory. Nevertheless, it still can be concluded that the prediction of cavity shapes using the theoretical formula is accurate enough for the penetration depth over twice the body length of water entry.

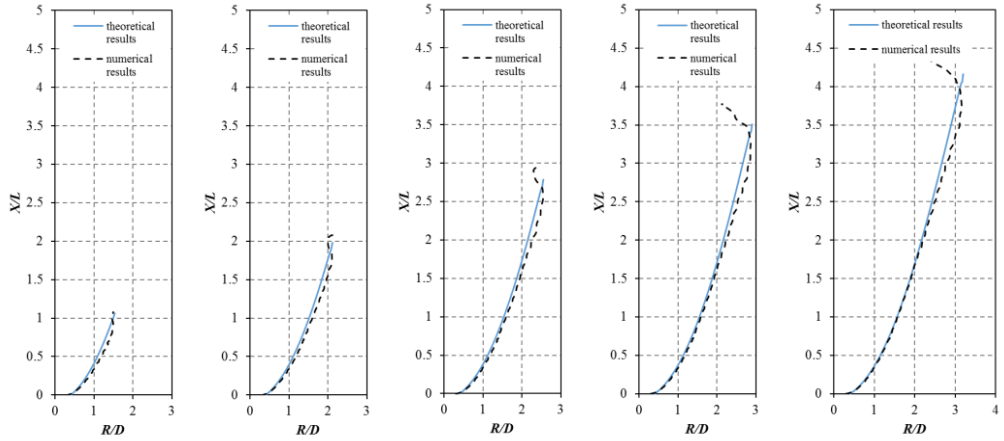

t=0.01s. t=0.02s. t=0.04s. t=0.04s. t=0.05s.

Figure 12: Comparisons of cavity shape between the numerical and theoretical results.

4.4 Similarity of high speed water entry

The process of high-speed water entry is unsteady and includes motion of multiple media including solid, air, vapour and water. The motion of the multiple media should be considered together. Meanwhile, the compressibility of air and water should also be considered in high-speed water entry. These factors make the problems of water-entry experiments quite complicated. Considering the parameters which may possibly influence the phenomenon of water-entry, the following relation can be assumed based on the dimensional analysis theory, as:

$$f(m,d,t,V_0,g,P_a,\rho_a,c_a,P_c,\rho_w,c_w,\mu,C_{D0}) = 0 \tag{12}$$

where m is the vehicle mass; d is the characteristic diameter; t is time from impact moment; V_0 is the water impact velocity; g is the gravity acceleration; P_a is the pressure of the air above the water; ρ_a is the air density above water; c_a is the sound speed of air; P_c is the cavity pressure; ρ_w is the water density; c_w is

the sound speed of water; μ is the viscosity of water, and C_{D0} is the drag coefficient of body at zero cavitation number.

For high-speed water-entry, the influences of viscosity and surface tension can be ignored. We select *m*, *d* and *t* as the fundamental quantities. According to Buckingham's pi-theorem, parameters in Eq. (12) can be combined into several independent non-dimensional groups shown as:

$$F\left(\frac{m}{\rho_w D^3}, \frac{V_0 t}{D}, \frac{V_0}{\sqrt{gD}}, \frac{V_0}{c_a}, \frac{V_0}{c_w}, \frac{P_a}{\frac{1}{2}\rho_w V_0^2}, \frac{P_c}{\frac{1}{2}\rho_w V_0^2}, \frac{\rho_a}{\rho_w}, C_{D0}\right) = 0 \tag{13}$$

The dynamic similarity will be achieved when all the non-dimensional parameters are equal for the model and prototype vehicle. However, all the similarity relations cannot be satisfied simultaneously during the experiments. We define the geometric scaling factor as $\lambda = d_p / d_m$, where the subscripts *p* and *m* refers to prototype and model respectively. In these factors, C_{D0} is only affected by the vehicle nose-shape; $m / \rho_w D^3$ is satisfied by model design; $V_0 t / D$ is only used in conversion from model to prototype; $P_c / 0.5\rho_w V_0^2$ is not an initial scaling factor. In general, water will not be changed to any other liquid for model test on the consideration of experimental costs, so V_0 / c_a and $P_a / 0.5\rho_w V_0^2$ are equivalent. Then, scaling factors can be reduced to:

$$\begin{cases} \text{Froude number: } Fr = V_0 / \sqrt{gD} \\ \text{Mach number: } Ma_w = V_0 / c_w \\ \text{Euler number: } Eu_a = P_a / 0.5\rho_w V_0^2 \\ \text{The density ratio: } \rho_a / \rho_w \end{cases} \tag{14}$$

Three scaling strategies are numerically studied in this paper to determine the relative importance of the scaling factors.

(1) Scalings of *Fr* and the density ratio are fulfilled, then $V_{0p} / V_{0m} = \sqrt{\lambda}$ and the air pressure above the water is not changed according to $P_{a,m} = P_{a,p}$, which means *Eu* and *Ma* are not fulfilled.

(2) Scalings of *Fr* and *Eu* are fulfilled, then $V_{0p} / V_{0m} = \sqrt{\lambda}$ and the air pressure above the water is changed according to $P_{a,m} = P_{a,p} / \sqrt{\lambda}$, which means *Ma* and the density ratio are not fulfilled.

(3) Scalings of *Ma*, *Eu* and density ratio are fulfilled, then $V_{0p} = V_{0m}$ and the air pressure above the water is not changed according to $P_{a,m} = P_{a,p}$, which means *Fr* is not fulfilled.

Fig. 13 shows the comparisons for different scale models with three scaling strategies. The drag coefficients, $C_D = F / 0.5\rho_w V_0^2$ and the relative pressure coefficients $C_P = (P - P_a) / 0.5\rho_w V_0^2$ were chosen to present the dynamic scaling of different scale models. In the calculations, models of three scales were used and the initial velocity of water-entry is 500m/s for the model with scale of 1. As shown in the figure, when the scaling of *Ma*, *Eu* and the density ratio are fulfilled, good scalings are obtained with different scale models. It can also be concluded that *Eu* is a relatively more important scaling factors than the density ratio when the scaling of *Ma* cannot be fulfilled by comparing the C_P in Fig. 13(a) and 13(b).

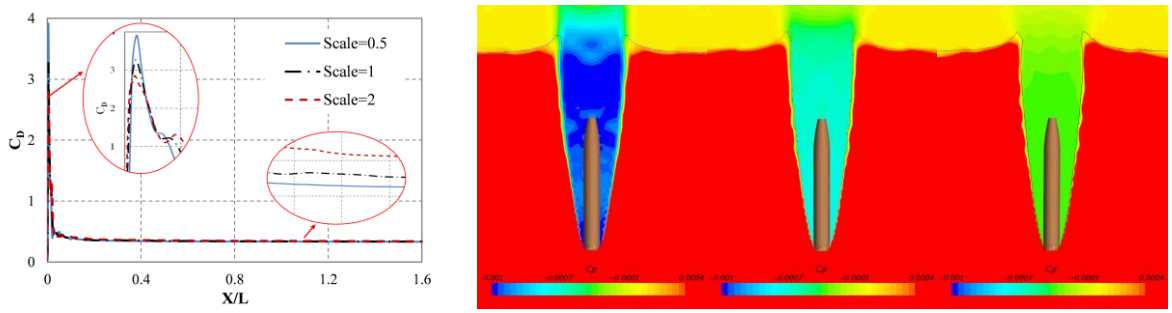

(a) Scalings of *Fr* and density ratio are fulfilled.

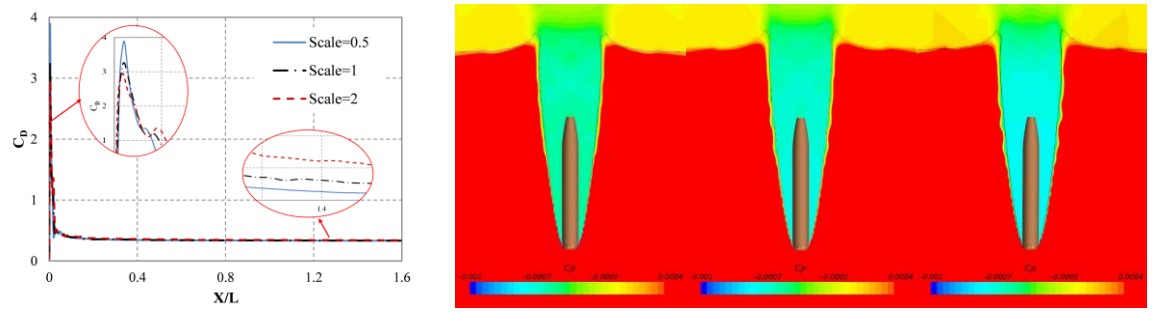

(b) Scalings of *Fr* and *Eu* are fulfilled.

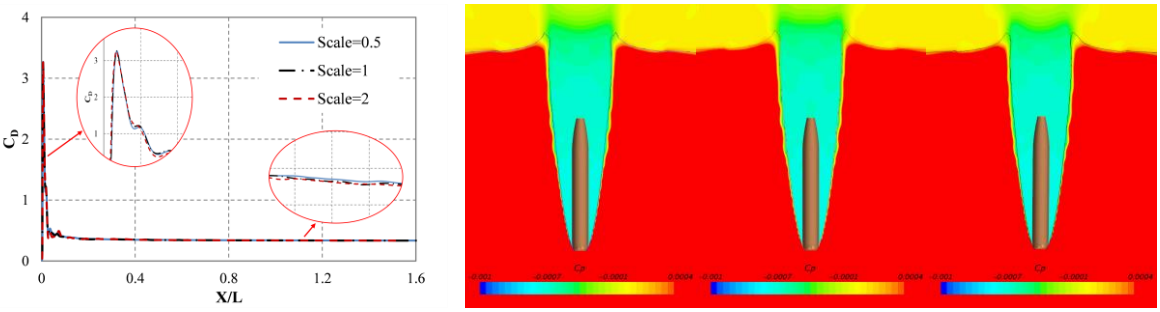

(a) Scalings of *Ma*, *Eu* and density ratio are fulfilled.

Figure 13: Comparisons of different scale models for three scaling strategies.
(*left: Drag coefficients, right: cavity pressure coefficients at the same dimensionless moment*)

5 CONCLUSIONS

In this paper, the water entry of an axisymmetric blunt vehicle with velocities ranging from 200m/s to 600m/s are numerically studied based on CFD method. Some problems in numerical simulations and experiments are discussed and following conclusions are obtained:

(1) The influence of water compressibility on the water entry is studied and it is found that the compressibility will affect impact loads and motions of water entry body but has little influence on cavity shapes.

(2) By comparing the numerical results of cavity shapes during early stages of water entry with the theoretical results based on the principle of independence of the cavity sections expansion, it is found that the numerical results of cavity shapes are generally agreed with theoretical results except for the parts near water surface.

(3) The main similarity parameters for high speed water entry are also analysed and it is concluded that Mach number is the most important similarity parameter during early stages of water entry at this range of velocities and Euler number is also a relative important similarity parameter for the scaling of pressure fields, when the scaling of *Ma* cannot be fulfilled.

ACKNOWLEDGEMENTS

We would like to thank National Supercomputing Center in Wuxi, China for providing the computing platform.

REFERENCES

[1] Zhonghan Yan. “On water entry of torpedo.” In: *Shipbuilding of China*, 43(3), 88-93, 2002. (in Chinese)

[2] May A. “*Water entry and the cavity-running behaviour of missiles.*” Tech. Rep. 20910, Naval Surface Weapons Center, White Oak Lab., MD, 1975.

[3] Shixing Yang, Naijin Li, Zhixuan Xu. *Air-dropped Torpedo technology*. Yunnan Science and Technology Press, 2001. (in Chinese)

[4] Von Karman, T. H. "*The impact on seaplane floats during landing.*" NACA Technical Note No. NACA-TN-32, 1929.

[5] Wagner, H. "*The phenomenon of impact and planning on water.*" NACA Technical Report 1366, 1932.

[6] Eroshin V.A., Romanenkov N.I., Serebryakov I.V., et al. "*Hydrodynamic forces produced when blunt bodies strike the surface of a compressible fluid*." In: *Mekhanika Zhidkostii Gaza*, 6: 44-51, 1979.

[7] Dobrovol'skaya, Z. N. "On some problems of similarity flow of fluid with a free surface." In: *Journal of Fluid Mechanics*, 36, 805–829, 1969

[8] Weiland C, Vlachos PP. "*Time-scale for critical growth of partial and supercavitation development over impulsively translating projectiles*." In: *International Journal of Multiphase Flow*, 38, 73–86, 2012.

[9] Korobkin, A. A. "*Blunt-body impact on the free surface of a compressible liquid.*" In: *Journal of Fluid Mechanics*, 263, 319–342, 1992.

[10] P. M. Aroson. "*An experimental investigation of cavity pressure scaling and drag coefficients encountered in the water entry of vehicles.*" Xerox University Microfilms, 1975

[11] *STAR-CCM+ user manual (2017): Version 12.02*, Siemens PLM Software Inc.

[12] McMillen, J. H. "*Shock Wave pressures in water produced by impact of small spheres*" In: Physical Review, 68(9–10), 198–309, 1945.

[13] Xuanzhi Xu. "*Torpedo Mechanics.*" National Defense Industry Press, Beijing, 1992.

[14] A. D. Vasin. "*The principle of independence of the cavity sections expansion (Logvinovich's principle) as the basis for investigation on cavitation flows*." In: RTO-AVT/VKI special course: supercavitating flows, von Karman Institute for Fluid Dynamics, Rhode-Saint-Genese, Belgium, 12–16, February, 2001.